Compensating Faraday Depolarization by Magnetic Helicity in the Solar Corona

Axel Brandenburg[1,2,3,4] , Mohira B. Ashurova[1,2] , and Sarah Jabbari[5]
[1] Laboratory for Atmospheric and Space Physics, University of Colorado, Boulder, CO 80303, USA; brandenb@nordita.org
[2] Department of Astrophysical and Planetary Sciences, University of Colorado, Boulder, CO 80303, USA
[3] Nordita, KTH Royal Institute of Technology and Stockholm University, Roslagstullsbacken 23, SE-10691 Stockholm, Sweden
[4] Department of Astronomy, AlbaNova University Center, Stockholm University, SE-10691 Stockholm, Sweden
[5] School of Mathematical Sciences and Monash Centre for Astrophysics, Monash University, Clayton, VIC 3800, Australia

Abstract

A turbulent dynamo in spherical geometry with an outer corona is simulated to study the sign of magnetic helicity in the outer parts. In agreement with earlier studies, the sign in the outer corona is found to be opposite to that inside the dynamo. Line-of-sight observations of polarized emission are synthesized to explore the feasibility of using the local reduction of Faraday depolarization to infer the sign of helicity of magnetic fields in the solar corona. This approach was previously identified as an observational diagnostic in the context of galactic magnetic fields. Based on our simulations, we show that this method can be successful in the solar context if sufficient statistics are gathered by using averages over ring segments in the corona separately for the regions north and south of the solar equator.

1. Introduction

The solar magnetic field has an opposite twist in the two hemispheres. This is seen, for example, in Hα images of the Sun through the orientation of sigmoidal structures of filaments in absorption. These structures are S-shaped in the south and N-shaped in the north, thus revealing a clear hemispheric dependence (Martin 2003). A similar dependence is also seen in the twist of force-free magnetic fields extrapolated from vector magnetograms around active regions (Seehafer 1990; Pevtsov et al. 1995). These indicate negative (positive) helicity in the northern (southern) hemisphere. The same hemispheric sign dependence was confirmed previously using magnetic helicity spectra that were computed from solar surface vector magnetograms (Zhang et al. 2016; Brandenburg et al. 2017).

Magnetic helicity spectra have also been computed from time series of the magnetic field vector measured on board the *Ulysses* spacecraft as it flew at high northern and southern heliographic latitudes (Brandenburg et al. 2011). However, the signs of magnetic helicity turned out to have the opposite sign of what is measured at the solar surface. This was rather surprising, although it could be understood as a consequence of a subdominance of generating effects (e.g., the α effect in dynamo theory) compared with dissipating effects (turbulent magnetic diffusion) in the solar wind. These two effects tend to affect the sign of magnetic helicity in opposite ways. In the convection zone, the α effect is dominant, but in the solar wind it is expected to be subdominant. This unusual sign reversal of magnetic helicity was then confirmed by Warnecke et al. (2011) using numerical simulations of a turbulent helical dynamo driven in the two hemispheres of a spherical wedge with a quiescent exterior. The current helicity, a proxy of magnetic helicity at small scales, was found to be positive (negative) in the northern (southern) hemisphere, i.e., just the other way around than in the dynamo region. They interpreted this in a slightly modified way by arguing that in the northern (southern) hemisphere, the dynamo sheds negative (positive) magnetic helicity through a turbulent diffusive helicity flux (Hubbard & Brandenburg 2011). Analogous to Fickian

diffusion of temperature, a flux is carried by a negative gradient, but here the magnetic helicity can have either sign. Thus, the negative magnetic helicity of the dynamo in the northern (southern) hemisphere is carried by a positive (negative) magnetic helicity gradient, driving it toward and arguably through zero. This would explain the opposite sign of magnetic helicity some distance above the solar surface. If this idea is indeed applicable to the Sun, it would be important to find out the distance above the solar surface, where the change of sign occurs. Could it be detected, for example, with Parker Solar Probe as it approaches the Sun down to 0.04 au, or could the sign reversal be measured within the solar corona (0.01 au), or perhaps even right at the solar surface?

Attempts to determine coronal magnetic helicity through morphological considerations and force-free extrapolations (Pariat et al. 2015; Valori et al. 2016) or by measuring helicity flux through the surface (Kazachenko et al. 2009) may be biased toward large scales. An alternate technique could utilize the effect of Faraday rotation along the line of sight. In the absence of magnetic helicity, a line-of-sight magnetic field leads to Faraday rotation and thus the superposition of polarization vectors with different orientations, which is called Faraday depolarization. A helical magnetic field of suitable sign can have the opposite effect and thus compensate Faraday depolarization and therefore increase the polarized intensity (Sokoloff et al. 1998; Brandenburg & Stepanov 2014; Horellou & Fletcher 2014). A helical field of opposite sign leads to a decrease in polarized intensity. Specifically, a line-of-sight magnetic field pointing toward (away from) the observer would decrease Faraday rotation, and thus enhance polarized intensity of a suitable wavelength, if the magnetic field has positive (negative) magnetic intensity (Brandenburg & Stepanov 2014). This result has been known in the galactic context, where the radiation is due to synchrotron emission. In the solar context, we have to rely on polarized radiation from magnetic-dipole transitions that occur in the corona at certain discrete wavelengths (Judge 1998; Casini & Judge 1999). Dove et al. (2011) proposed the use of polarized emission to infer the twisted nature of coronal magnetic fields

through forward modeling of the Stokes vector and comparing against measurements with the Coronal Multichannel Polarimeter (CoMP) telescope (Tomczyk et al. 2008; Dima et al. 2016; Gibson et al. 2017). However, Faraday rotation was not invoked in their approach, which would require longer wavelengths in the millimeter range, as will be shown below.

For the Sun, using narrow bandwidth observations at $\lambda = 6$ cm radio wavelengths, Alissandrakis & Chiuderi-Drago (1994) found an oscillatory variation of the Stokes Q and U parameters with respect to small changes in λ. However, those wavelengths are too long to determine magnetic helicity. Furthermore, we also need the line-of-sight magnetic field, because it determines the Faraday depolarization. This can be obtained by determining the rotation measure, i.e., the derivative of the polarization angle with respect to wavelength, giving the sign of the toroidal magnetic field. This is another standard concept used mainly in radio astronomy, but it applies to other wavelengths as well. The correlation between rotation measure and polarized intensity is therefore a direct proxy of magnetic helicity and was first proposed by Volegova & Stepanov (2010). We emphasize that with our technique the actual orientation of the transverse component of the magnetic field is not important. It is only the *change* of the orientation with increasing distance from the observer that enters. In particular, no background sources are invoked and only the radiation from within the corona is used. The purpose of this Letter is to discuss the feasibility of this technique in the solar context and to apply it to a simple model such as that of Warnecke et al. (2011, 2012).

2. Description of the Method

The simplest example we can construct is that of a Beltrami field, which Brandenburg & Stepanov (2014) wrote as $(B_x, B_y, B_z) = (B_\perp \sin kz, \, B_\perp \cos kz, \, 0)$, where the observer is in the negative z direction. Here, k is the wavenumber of the magnetic field. They expressed the component perpendicular to the direction of the observer $\boldsymbol{B}_\perp = (B_x, B_y)$ in a complex form as $\mathcal{B} \equiv B_x + iB_y = r_B \exp(i\psi_B)$. In the present arrangement, the observer is in the negative y direction, so we rotate $z \rightarrow y$, $B_y \rightarrow B_x$, and $B_x \rightarrow B_z$, so we have

$$\boldsymbol{B} = \begin{pmatrix} B_x \\ B_y \\ B_z \end{pmatrix} = \begin{pmatrix} B_\perp \cos ky \\ B_{\|0} \\ B_\perp \sin ky \end{pmatrix}, \qquad (1)$$

with $\boldsymbol{B}_\perp = (B_x, B_z)$ and $\mathcal{B} \equiv B_z + iB_x = r_B \exp(i\psi_B)$. We have assumed here a constant line-of-sight magnetic field, $\boldsymbol{B}_\| = (0, B_{\|0}, 0)$. The intrinsic linear polarization vector (q, u) is then

$$q + iu = p_0 \, \epsilon \, \exp(2i\psi_p), \qquad (2)$$

where $\psi_P = \psi_B + \pi/2$ is the electric field angle, $\epsilon(x, y, z)$ is the emissivity, and p_0 is the degree of polarization. Integrating along the line of sight yields the observable polarization, written here in complex form as

$$P(x, z, \lambda^2) \equiv Q + iU = p_0 \int_{-\infty}^{\infty} \epsilon \, e^{2i(\psi_P + \phi\lambda^2)} \, dy, \qquad (3)$$

Table 1
Wavelength λ of Maximum Polarized Emission for Fully Helical Magnetic Fields with $k = 0.01$ Mm$^{-1} = 1500$ au^{-1} for n_e [cm^{-3}] and $B_\|$ [G]

$B_\|$	n_e				
	10^6	10^8	10^{10}	10^{12}	10^{14}
0.01 G	20 cm	2 cm	2 mm	200 μm	20 μm
1 G	2 cm	2 mm	200 μm	20 μm	2 μm
100 G	2 mm	200 μm	20 μm	2 μm	200 nm

where λ is the wavelength,

$$\phi(x, y, z) = -K \int_{-\infty}^{y} n_e(x, y', z) B_\|(x, y', z) dy' \qquad (4)$$

is the Faraday depth, with n_e being the electron density and $K = 0.81$ m^{-2} cm^3 μG^{-1} pc$^{-1} = 2.6 \times 10^{-17}$ G^{-1} being a constant (e.g., Alissandrakis & Chiuderi-Drago 1994). As in Brandenburg & Stepanov (2014), we assume $\epsilon \propto B_\perp^\sigma$ and compare $\sigma = 2$ and 0. Furthermore, we normalize P by the total intensity $I = \int \epsilon \, dy$. Of particular interest is the case when the polarized emission is maximum, which is when the exponent in Equation (3) vanishes. Equation (4) applies to nonuniform n_e and $B_\|$, but we now discuss the case when $n_e = n_{e0}$ and $B_\| = B_{\|0}$ are constants. A fully helical magnetic field of the form given by Equation (1) makes the exponent vanish if $\psi_B - \pi/2 = -ky$, i.e., if the wavenumber of the field in Equation (1) obeys

$$k = -Kn_{e0}B_{\|0}\lambda^2. \qquad (5)$$

In that case, Faraday depolarization becomes minimal, i.e., we have maximum polarization. This is the essence of this technique.

To get an idea about the ranges in λ and n_e that would be needed to obtain cancelation for a magnetic field of wavenumber $k = 0.01$ Mm$^{-1} = 1500$ au^{-1}, which corresponds to a length scale of $(2\pi/0.01)$ Mm ≈ 600 Mm, we have listed plausible combinations of n_e, λ, and $B_\|$ in Table 1. This wavenumber lies on the lower end of values relevant to the solar surface (Brandenburg et al. 2017) and near the upper end of values in the solar wind (Brandenburg et al. 2011). Thus, the far- to near-infrared wavelength range is optimal for detecting helical magnetic fields. On a scale of 60 Mm, all wavelengths would be three times larger. To discuss the feasibility of this method further, we determine the line-of-sight integrated polarization using the magnetic field from a simulation similar to that of Warnecke et al. (2011).

3. Numerical Simulations

We solve the hydromagnetic equations for the magnetic vector potential $\boldsymbol{A}$, the velocity $\boldsymbol{U}$, and the logarithmic density $\ln \rho$, using an isothermal equation of state with constant sound speed c_s:

$$\frac{\partial \boldsymbol{A}}{\partial t} = \boldsymbol{U} \times \boldsymbol{B} - \eta\mu_0\boldsymbol{J}, \qquad (6)$$

$$\frac{D\boldsymbol{U}}{Dt} = \boldsymbol{g} + \boldsymbol{f} - c_s^2\boldsymbol{\nabla}\ln\rho + \frac{1}{\rho}[\boldsymbol{J} \times \boldsymbol{B} + \boldsymbol{\nabla} \cdot (2\nu\rho\mathsf{S})], \qquad (7)$$

$$\frac{D\ln\rho}{Dt} = -\boldsymbol{\nabla} \cdot \boldsymbol{U}, \qquad (8)$$

2

where $\boldsymbol{B} = \boldsymbol{\nabla} \times \boldsymbol{A}$ is the magnetic field, $\boldsymbol{J} = \boldsymbol{\nabla} \times \boldsymbol{B}/\mu_0$ is the current density, μ_0 is the magnetic permeability, ν is the kinematic viscosity, $\mathsf{S}_{ij} = \frac{1}{2}(U_{i,j} + U_{j,i}) - \frac{1}{3}\delta_{ij}\boldsymbol{\nabla} \cdot \boldsymbol{U}$ is the rate-of-strain tensor, $\boldsymbol{g}$ is the gravitational acceleration, and $\boldsymbol{f}$ is a forcing function; see below.

We consider a wedge-shaped computational domain in spherical coordinates (r, ϑ, φ) with

$$0.7 \leqslant r/R \leqslant 2, \quad 15° \leqslant \vartheta \leqslant 165°, \quad -17°\!.5 < \varphi < 17°\!.5, \tag{9}$$

where R is the solar radius. The gravitational acceleration is $\boldsymbol{g} = (-GM/r^2, 0, 0)$, where G is Newton's constant and M is the solar mass. We use $GM/(Rc_s^2) = 3$, which results in a density contrast of about 16 in the radial direction. As in Warnecke et al. (2011), $\boldsymbol{f}$ consists of plane waves with typical wavenumber $k_f = 3k_0$ and is nonvanishing only in the "turbulence zone" in $0.7 \leqslant r/R \leqslant 1$. Here, $k_0 = 2\pi/(0.3\,R)$ is the lowest radial wavenumber in this zone of thickness $0.3\,R$. The helicity of $\boldsymbol{f}$ changes sign about the equator and is negative (positive) in the northern (southern) hemisphere. We use the PENCIL CODE[6] in spherical wedge geometry with $144 \times 288 \times 72$ mesh points in the r, ϑ, and φ directions.

The magnetic field grows at first exponentially with time at a growth rate $\gamma \approx 0.073\,\tau^{-1}$, where $\tau = (u_{rms}k_f)^{-1}$ is the turnover time in the dynamo region of our model and is about $\tau = 0.14\,R/c_s$. The magnetic field develops a cycle with equatorward migration. The period is about $2000\,\tau$, which is about 10 times longer than for the smaller wedges of Warnecke et al. (2011), which spanned $\pm18°$ latitude. Such migratory dynamos without differential rotation were discovered by Mitra et al. (2010). In contrast to earlier work (Warnecke et al. 2011, 2012), we have now extended the latitude range to $\pm75°$. Models with this latitudinal extent, but no corona, where also studied by Jabbari et al. (2015), who investigated the spontaneous formation of spots at the surface in the presence of dynamo action, but at much larger stratification.

Our model is different from the standard scenario of a solar dynamo, which involves differential rotation. One reason for adopting an α^2 dynamo is its simplicity, while capturing essential features of a realistic turbulent dynamo: scale separation, different signs of magnetic helicity at large and small scales, and magnetic helicity fluxes out of the domain and across the equator. As a model for the Sun, such a dynamo is not implausible (Käpylä et al. 2013; Masada & Sano 2014). However, as we will see below, in our model the magnetic field is strongest at high latitudes. This could in principle be alleviated by adopting a modified helicity profile, as done in Jabbari et al. (2015). Such refinements, as well as the inclusion of differential rotation, would be useful extensions for future work.

4. Calculation of the Line-of-sight Magnetic Field

To perform line-of-sight integrations as in Equations (3) and (4), we overlay a Cartesian mesh with coordinates (x, y, z) and look up at each Cartesian meshpoint the nearest magnetic field value on the spherical mesh at position (r, ϑ, φ). The components of $\boldsymbol{B} = (B_r, B_\vartheta, B_\varphi)$ are then expressed in terms of Cartesian components. As in Section 2, the observer is assumed

---
6 https://github.com/pencil-code
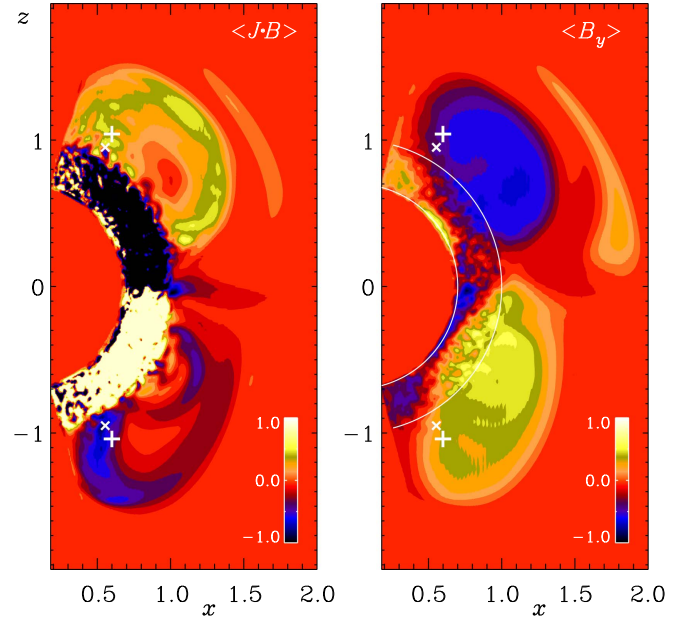
Figure 1. $\langle \boldsymbol{J} \cdot \boldsymbol{B} \rangle_y$ (left) and $\langle B_y \rangle_y$ (right) at $t/\tau = 430$. The crosses and plusses mark positions at $r/R = 1.1$ and 1.2 and $90° - \vartheta = \pm60°$ latitude, for which the λ^2 dependence is studied in Figure 2.

to be looking in the positive y direction. Thus, $B_\varphi > 0$ implies positive $B_\parallel = B_y$ in the first or fourth quadrants, which corresponds to negative Faraday depth; see Equation (4).

In Figure 1, we plot the current helicity $\langle \boldsymbol{J} \cdot \boldsymbol{B} \rangle_y$ and mean toroidal field $\langle B_y \rangle_y$, where $\langle \cdot \rangle_y$ denotes averaging along the line of sight. In $r < R$, $\langle \boldsymbol{J} \cdot \boldsymbol{B} \rangle_y$ is negative (positive) in the northern (southern) hemisphere, but it changes sign for $r > R$ and becomes positive (negative) in the northern (southern) hemisphere. Furthermore, $\langle B_y \rangle_y$ is negative in the first quadrant (northern hemisphere), so the Faraday depth is positive; see Equation (4).

Figure 1 shows that in the northern hemisphere, the coronal magnetic field has positive $\langle \boldsymbol{J} \cdot \boldsymbol{B} \rangle_y$. This is consistent with the results of Warnecke et al. (2011) and, since current helicity is a proxy of small-scale magnetic helicity, it is also consistent with the results for the solar wind (Brandenburg et al. 2011). Let us now ask whether this result can also be inferred from the polarized intensity computed from our models using Equation (3). We begin by plotting $|P(\lambda^2)|$ at points where the field is strongest. As alluded to at the end of Section 3, this is in our model at high latitudes, so we choose four reference points at $\pm60°$ latitude at $r/R = 1.1$ and 1.2 indicated in the two panels of Figure 1. The result is shown in Figure 2(a), where we have normalized $|P|$ by the total intensity I at the same point, and λ^2 is normalized by

$$\lambda_0^2 \equiv (Kn_{e0}B_{\parallel 0}R)^{-1}, \tag{10}$$

which implies that $\lambda^2/\lambda_0^2 = kR$. In this case, the values of λ given in Table 1 are somewhat smaller: 0.75 cm instead of 2 cm, for example.

We see from Figure 2(a) that, in the northern hemisphere, the polarized intensity has a maximum at a positive value of λ^2/λ_0^2. This is consistent with our expectation that for positive Faraday depth, i.e., negative B_φ, polarized intensity should be maximum for positive values of λ^2 if the magnetic helicity is positive (Brandenburg & Stepanov 2014). In the southern hemisphere, Equation (3) shows that the polarized intensity has a maximum
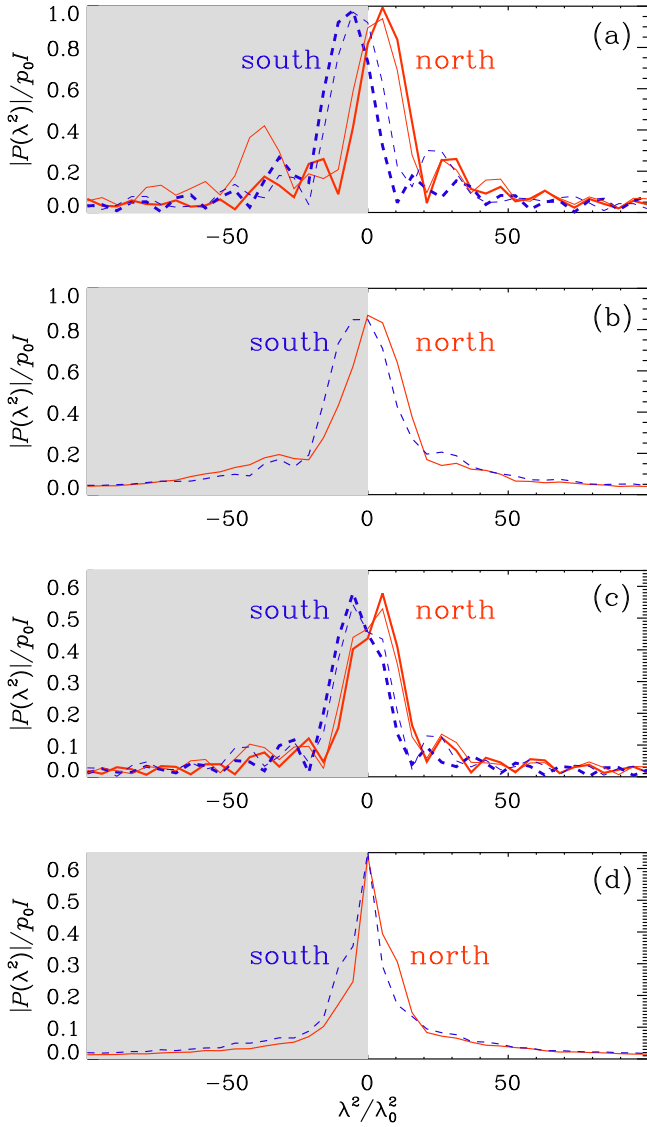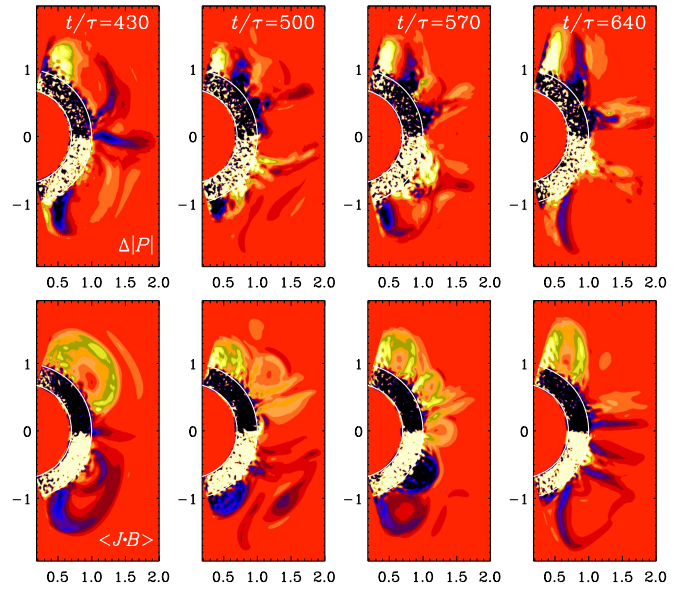
Figure 2. (a) $|P(\lambda^2)|$ at four reference points indicated in the two panels of Figure 1 in the northern (red) and southern (blue) hemispheres at $t/\tau = 430$. Thick (thin) lines refer to $r/R = 1.2$ (1.1) at $\pm 60°$ latitude. (b) $|P(\lambda^2)|$ averaged over radial shells, $r/R = 1.10$–1.15. Shaded areas denote $\lambda^2 < 0$, which are unphysical. ((c) and (d)) Same as (a) and (b), but for $\sigma = 0$.

Figure 3. $\Delta|P|$ (upper row) and $\langle \boldsymbol{J} \cdot \boldsymbol{B} \rangle$ in the xz plane of the observer at four times in the interval $t/\tau = 430$–640. The color table is the same as in Figure 1.

correspondence between polarized intensity and current helicity are not uncommon. Therefore, a more robust method is to use hemispheric ring averages, $\langle |P| \rangle_{(N/S)}$, which are averages of $|P(r, \theta)|$ over an interval $r_1 < r < r_2$ and $0 < \theta < \pi/2$ for the north (N) and $\pi/2 < \theta < \pi$ for the south (S). The result is shown in Figure 2(b) for a ring with $r_1/R = 1.10$ and $r_2/R = 1.15$. The difference in polarized intensity for north and south is now no longer so striking, but it may well be good enough if sufficient statistics are gathered.

Incidentally, Figure 2(a) also shows oscillations in the wings at larger values of λ^2 with $\Delta \lambda^2 \approx 20 \lambda_0^2$. This is a consequence of the finiteness of nonvanishing contributions to the integral in Equation (3) for a finite slab (Burn 1966). Such oscillations have indeed been observed by Alissandrakis & Chiuderi-Drago (1994) using radio observations of the solar corona at a small bandwidth at 6 cm wavelength. In our simulation, this corresponds to a slab of width $L = 2\pi R/20 \approx 0.3\, R$, which agrees with our domain size along the line of sight.

To demonstrate the relationship between helicity and polarized intensity more thoroughly, we now consider an artificially constructed quantity

$$\Delta|P| \equiv \langle |P| \rangle_+ - \langle |P| \rangle_-, \qquad (11)$$

where the $\langle |P| \rangle_\pm$ denote the averages of $|P|$ over the intervals $0 < \lambda^2/\lambda_0^2 < 60$ and $-60 < \lambda^2/\lambda_0^2 < 0$, respectively Again, the negative λ^2 interval is of course unobservable in reality, but computing it from our models allows us to see more clearly the degree of correspondence with the $\langle \boldsymbol{J} \cdot \boldsymbol{B} \rangle$ maps. In Figure 3, we show $\Delta|P|$ for four times separated by $70\, \tau$ around the times considered above. The visualizations of $\Delta|P|$ are found to be a reasonable proxy of $\langle \boldsymbol{J} \cdot \boldsymbol{B} \rangle$ inside the turbulence zone ($r < R$), but in the corona $\Delta|P|$ is no longer a good proxy—at least not at all times. This, again, highlights the need for using averages to obtain reliable results.

at negative values of λ^2, which is of course unphysical and unobservable. However, even in that case, the integral in Equation (3) can still be evaluated. In fact, it is well known that this integral is just the usual Fourier integral provided the integration is performed over ϕ instead of y (Burn 1966; Brentjens & de Bruyn 2005). If B_φ were positive (e.g., half a Hale cycle later), one should see more polarized intensity in the south instead.

Figure 2(a) shows that the maximum of $|P|/I$ is at $\lambda^2/\lambda_0^2 \approx 5$, i.e., $\lambda/\lambda_0 \approx 2.2$. For the Sun, at $r/R = 1.1$, we expect $n_e = 10^{-8}\, \mathrm{cm}^{-3}$. Using $B_{\parallel 0} = 1$ G, as an example, we have $\lambda_0 \approx 2$ mm, so $\lambda \approx 4$ mm, which is at the limit of ALMA. In the outer parts, n_e would be lower, so λ would be larger still. The results for $\sigma = 0$ are similar to those for $\sigma = 1$; see Figures 2(c) and (d).

Looking only at one position in the corona may not be enough to get a reliable result about the coronal magnetic helicity. In fact, as we will see further below, exceptions to the

5. Conclusions

Our results have confirmed that there is a correspondence between polarized intensity and magnetic or current helicity.

This idea was originally applied to galaxies, but it should also work for the Sun using polarized emission from within the corona some distance above the solar surface. The most appropriate wavelengths lie in the millimeter range, which has only now become accessible through ALMA.

Using studies of polarized intensity to constrain the solar dynamo and magnetic helicity in the corona may shed light on the nature of the dynamo mechanism, which is likely to involve an α effect as a result of cyclonic convection, as anticipated already by Parker (1955). Such a dynamo produces helical magnetic fields through an inverse cascade of magnetic helicity (Pouquet et al. 1976). However, unlike kinetic helicity, magnetic helicity is conserved and both positive and negative signs tend to be produced at the same time, but at different length scales. Different signs of magnetic helicity are also present in the solar wind at large and small scales. Brandenburg et al. (2011) associated the helicity at the largest scales with that of the Parker spiral (Parker 1958), which is negative in the north (Bieber et al. 1987). At smaller scales, the sign of magnetic helicity in the solar wind agrees with that at large scales in the dynamo interior. Our new simulations suggest that the apparent sign reversal may occur close to the solar surface; see the lower panel of Figure 3. This raises our hopes that further guidance for our understanding of this effect can come from observations.

In the present work, we have examined the possibility of using the compensating effect of a helical magnetic field on Faraday rotation. This idea has not yet received much attention in solar physics, except for early work of the 1990 s that showed the essence of Faraday rotation at radio wavelengths (Alissandrakis & Chiuderi-Drago 1994). These authors considered observations on the solar disk above active regions, but solar limb observations appear plausible too. It is essential to use a broad range of wavelengths from infrared to millimeter wavelengths. However, the actual location of this helicity reversal should be treated with care. It is therefore essential to inspect a suitable range of data using not only ALMA and CoMP observations, but also in situ observations using, for example Parker Solar Probe to inspect statistical properties of the field at close range.

ORCID iDs

Axel Brandenburg https://orcid.org/0000-0002-7304-021X
Mohira B. Ashurova https://orcid.org/0000-0002-8016-400X
Sarah Jabbari https://orcid.org/0000-0003-4039-5839

References

Alissandrakis, C. E., & Chiuderi-Drago, F. 1994, ApJL, 428, L73
Bieber, J. W., Evenson, P. A., & Matthaeus, W. H. 1987, ApJ, 315, 700
Brandenburg, A., Petrie, G. J. D., & Singh, N. K. 2017, ApJ, 836, 21
Brandenburg, A., & Stepanov, R. 2014, ApJ, 786, 91
Brandenburg, A., Subramanian, K., Balogh, A., & Goldstein, M. L. 2011, ApJ, 734, 9
Brentjens, M. A., & de Bruyn, A. G. 2005, A&A, 441, 1217
Burn, B. J. 1966, MNRAS, 133, 67
Casini, R., & Judge, P. G. 1999, ApJ, 522, 524
Dima, G., Kuhn, J., & Berdyugina, S. 2016, FrASS, 3, 13
Dove, J. B., Gibson, S. E., Rachmeler, L. A., Tomczyk, S., & Judge, P. 2011, ApJL, 731, L1
Gibson, S. E., Dalmasse, K., Rachmeler, L. A., et al. 2017, ApJL, 840, L13
Horellou, C., & Fletcher, A. 2014, MNRAS, 441, 2049
Hubbard, A., & Brandenburg, A. 2011, ApJ, 727, 11
Jabbari, S., Brandenburg, A., Kleeorin, N., Mitra, D., & Rogachevskii, I. 2015, ApJ, 805, 166
Judge, P. G. 1998, ApJ, 500, 1009
Käpylä, P. J., Mantere, M. J., Cole, E., Warnecke, J., & Brandenburg, A. 2013, ApJ, 778, 41
Kazachenko, M. D., Canfield, R. C., Longcope, D. W., et al. 2009, ApJ, 704, 1146
Martin, S. F. 2003, AdSpR, 32, 1883
Masada, Y., & Sano, T. 2014, ApJL, 794, L6
Mitra, D., Tavakol, R., Käpylä, P. J., & Brandenburg, A. 2010, ApJL, 719, L1
Pariat, E., Valori, G., Démoulin, P., & Dalmasse, K. 2015, A&A, 580, A128
Parker, E. N. 1955, ApJ, 122, 293
Parker, E. N. 1958, ApJ, 128, 664
Pevtsov, A. A., Canfield, R. C., & Metcalf, T. R. 1995, ApJL, 440, L109
Pouquet, A., Frisch, U., & Léorat, J. 1976, JFM, 77, 321
Seehafer, N. 1990, SoPh, 125, 219
Sokoloff, D. D., Bykov, A. A., Shukurov, A., et al. 1998, MNRAS, 299, 189
Tomczyk, S., Card, G. L., Darnell, T., et al. 2008, SoPh, 247, 411
Valori, G., Pariat, E., Anfinogentov, S., et al. 2016, SSRv, 201, 147
Volegova, A. A., & Stepanov, R. A. 2010, JETP, 90, 637
Warnecke, J., Brandenburg, A., & Mitra, D. 2011, A&A, 534, A11
Warnecke, J., Brandenburg, A., & Mitra, D. 2012, JSWSC, 2, A11
Zhang, H., Brandenburg, A., & Sokoloff, D. D. 2016, ApJ, 819, 146